Influence of the substrate, metal overlayer and lattice neighbors on the focusing properties of colloidal microspheres

Nikita Arnold

Abstract Calculations of the field distribution in colloidal SiO$_2$ microspheres are presented. Two cases are considered: small particles on a Si substrate irradiated by the 266 nm light, and larger ones, covered with a gold film and irradiated at 800 nm. Substrate, neighboring spheres and sputtered metal overlayer all significantly modify the field pattern and magnitude. Reflected light is focused inside the spheres, which may lead to their damage. The results can be useful in the analysis of microspheres-assisted nano-patterning.

PACS 42.62.-b · 42.25.Fx · 81.16.Mk · 81.65.Cf · 42.25.Bs

1 Introduction

Arrays of colloidal silica and polystyrene microspheres deposited on a silicon substrate [1–3] or self-assembling on a transparent quartz support [4, 5] were used lately for nano-patterning of surfaces upon irradiation by laser light. The arrangement with the transparent support allows one to vary the distance between the array and the substrate, as well as to deposit overlayers of Si and/or metal onto the top of the spheres [6–8]. These experiments attracted attention to the focusing properties of such microspheres. The focusing by the single spheres was studied on the basis of Mie theory

N. Arnold (✉)
Institute of Applied Physics, J. Kepler University,
Altenbergerstrasse 69, 4040 Linz, Austria
e-mail: nikita.arnold@jku.at

Present address:
N. Arnold
Institute of Experimental Physics, J. Kepler University,
Altenbergerstrasse 69, 4040 Linz, Austria

[9], its particle-on-surface extension [10], and analytical approximations for the small and large spheres [11, 12], in the latter case using uniform asymptotics of physical optics. Interference patterns produced by multiple spheres were discussed in [5] on the basis of Gaussian beam approximation. Transmission properties and photonic modes excited in the monolayer (ML) of spheres with different overlayers were studied in [6, 13].

In real experiments, the influence of the nearest neighbors on the focusing properties [5, 14], and the presence of strongly reflecting surfaces—for example Si substrate or metallic overlayer [7, 8]—are often of importance. These factors are difficult to reliably account for analytically, especially with multiple spheres of moderate Mie parameters, when all approximations work poorly.

In this work we present finite difference time domain (FDTD) calculations of the field distributions for single and multiple microspheres lying on a substrate or covered by a thin metal layer. Emphasis is placed on the main differences with the case of an isolated sphere and, on providing simple estimations for the influence of these factors. As an example we consider SiO$_2$ microspheres either on a Si substrate, irradiated at wavelength $\lambda = 266$, or covered by Au and irradiated at 800 nm. In addition, the influence of the capillary condensation in the sphere-substrate interstice is considered for the former case.

2 Single sphere

Let us first outline the field enhancement effects for the sole (transparent) sphere with the radius a and refractive index n. A sphere much smaller than the wavelength can be treated as a dipole with the known polarizability. This results in the
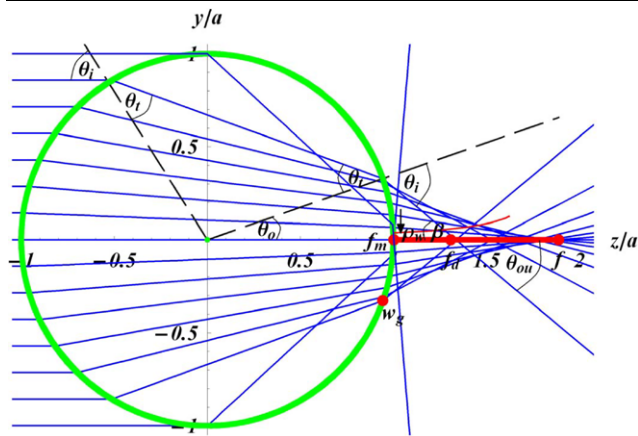
Fig. 1 Focusing properties for a single microsphere. Light propagates from left to right. Refractive index $n = 1.36$, Mie parameter $ka = 62.8$, which corresponds to $a = 10\lambda$. *Dots* indicate the following points: f—geometrical focus, f_d—diffraction focus, f_m—marginal focus, and w_g is the radius of the caustic cusp on the sphere. f_m can be both inside and outside the sphere, depending on the value of n (see text). Angles of incidence θ_i, refraction θ_t, as well as θ_o and θ_{ou} explained in the text, and the angle with the z-axis, β, are all indicated for some representative ray which passes closely to both w_g and f_d. *Thin curve* above the z-axis indicates local width of the focal line ρ_w. The caustic focal line extends from f_m to f

intensity enhancement proportional to the $(ka)^2$ [11]. Here k is the vacuum wavevector.

Larger spheres of several wavelengths in diameter act as strongly aberrated lenses and even the qualitative features of the field distribution can be understood only when taking this into account [15]. Here, analytical approach based on the uniform asymptotics of geometrical optics has been developed [12]. The ray picture is shown in Fig. 1. It reveals the caustic cusp (where the meridional radius of wavefront curvature changes its sign) and caustic "focal" line along the z-axis (where the cone of non-paraxial rays intersects and the sagittal radius of curvature goes through zero). All the distances shall be counted from the sphere center where both principal planes lie. Both the caustic line and the cusp end at the geometrical-optics focus, given by

$$f = \frac{a}{2}\frac{n}{n-1}. \tag{1}$$

To estimate the parameters of the cusp we note, that according to Snell's law, the ray with the incidence angle θ_i has the refraction angle inside the sphere $\theta_t = \arcsin(\sin(\theta_i)/n)$. Upon second refraction it leaves the sphere at a point with the polar angle (from z axis) $\theta_o = 2\theta_t - \theta_i$, and emerges from the sphere in the direction $\theta_{ou} = 2\theta_t - 2\theta_i < 0$. The ray that touches the caustic exactly on a sphere is the farthest from the z-axis there and therefore requires that $\theta_o(\theta_i)$ has its maximal value. From this condition one finds that $\sin^2\theta_i = (4 - n^2)/3$, and for the caustic point on the sphere

$\sin^2\theta_o = \frac{(4-n^2)^3}{27n^4}$. Thus, the caustic *cusp* radius *on the sphere* is given by

$$w_g = a\sin\theta_o = a\left(\frac{(4-n^2)}{3n^{4/3}}\right)^{3/2}. \tag{2}$$

At the caustic surface the field changes from the oscillating one in the lit area to the exponentially decaying evanescent field in the shadow region (the region with one ray instead of three in the case of a sphere). Due to continuity this shifts the maximum caustic intensity into the lit region. As explained in [16], the shift distance $\delta w_g \sim \lambda^{2/3}a^{1/3}$.

The caustic *focal line* starts at the point f_m (marginal focus [17]) where the outermost ray with $\theta_i = \pi/2$ crosses the z-axis. In this case $\sin\theta_t = 1/n$ (total internal reflection angle with vanishing transmission) and $\sin\theta_o = \sin(2\theta_t - \pi/2) = 2/n^2 - 1$. Thus, one has to distinguish between the two cases: $n > \sqrt{2}$, when $\sin\theta_o < 0$, and the focal line starts inside the sphere, and $n < \sqrt{2}$ when it starts outside, namely at

$$f_m = \frac{a}{\cos\theta_o} = \frac{a}{2}\frac{n^2}{\sqrt{n^2-1}}. \tag{3}$$

As the focal line has high intensity $I \propto ka$ everywhere, this has implications for laser processing employing the microspheres, especially when they are deposited directly onto the processed surface. For example, large polystyrene (PS) spheres with $n \sim 1.6$ shall have significantly higher peak enhancement *near the surface* than SiO$_2$ spheres with $n \sim 1.36$, for which the caustic line does not reach the sphere.

The intensity along the focal line oscillates due to interference between the axial ray with the phase φ_a and the cone of abaxial sagittal rays with equal phases φ_{ab}, converging at the given point of z-axis [12]. The global maximum (diffraction focus f_d) is given by the first constructive interference between these two terms. Abaxial rays acquire caustic phase shift of $-\pi/2$ as they touch the caustic cusp. This is the "delay" due to change in sign of meridional divergence. They acquire a further shift of $-\pi/2$ when crossing the focal line (change in sagittal divergence). But exactly *on the axis* only half of this delay has occurred. This yields the condition $\varphi_{ab} - \varphi_a = 3\pi/4$ for the global maximum. In the lowest order of the inverse product ka one can obtain the correction to the geometrical focus f

$$f_d = f\left(1 - \sqrt{\frac{3\pi}{4ka}\frac{n(3-n)-1}{n(n-1)}}\right). \tag{4}$$

Another important parameter is the variable convergence angle of the abaxial rays' cone $\beta \equiv -\theta_{ou}$. As explained in [12], it determines the local fine structure of the caustic line and therefore the localization of laser-induced patterns. For example the local width of the focal line ρ_w (radius till the first

zero) can be estimated from the condition that two abaxial rays interfere destructively. Taking into account caustic shift for the ray that crossed the focal line, one obtains $\varphi_{ab1} - \varphi_{ab2} = \pi + \pi/2$, from which $\rho_w \approx \frac{3}{8} \frac{\lambda}{\sin\beta}$ follows.

For the typical values of n, the angle β near the sphere surface is quite large and the axial component of the electric field E_z dominates. On the axis E_z components from the two symmetric abaxial rays point into the opposite directions and cancel, having an effective phase difference of $-\pi$. Off-axis, the ray that crossed the focal line underwent a caustic phase shift of $-\pi/2$, which makes the *purely geometrical* phase difference for constructive interference equal to $3\pi/2$. This results in the double-peak structure of the field in the direction of polarization, which was observed experimentally [18, 19]. The peaks occur at radial distance $\rho_p \approx \frac{3}{8} \frac{\lambda}{\sin\beta}$. As $E_z = 0$ on the axis, this is also the radius of each peak as well as the typical full width at half maximum (FWHM) for the field. Intensity distribution is narrower by a factor of $\sqrt{2}$. The analysis in [12, 20] yields the somewhat lower value 0.293 instead of $3/8 = 0.375$. This is smaller than the (scalar) Airy spot for the ideal lens with the same aperture angle β, where similar coefficient is 0.61 [17]. Large angles β are routinely realized near the sphere surface. Indeed, with $n < \sqrt{2}$ the outermost ray with $\theta_i = \pi/2$ at $z = f_m$ has the following angle with z-axis (see (3)):

$$\sin\beta \equiv \sin(-\theta_{ou}) = \sin(\pi - 2\theta_t) = 2\sqrt{n^2-1}/n^2. \quad (5)$$

With $n > \sqrt{2}$ the ray of interest leaves the sphere at $z = a$. For such a ray $\theta_o = 2\theta_t - \theta_i = 0 \Rightarrow 2\sin\theta_t \cos\theta_t = \sin\theta_i = n\sin\theta_t \Rightarrow \cos\theta_t = n/2$. In this case

$$\sin\beta \equiv \sin(-\theta_{ou}) = \sin(2\theta_i - 2\theta_t) = \sin\theta_i = n\sin\theta_t$$

$$= n\sqrt{1 - n^2/4}. \quad (6)$$

With these approximations $\sin\beta > 0.9$ for $1.18 < n < 1.69$. Clearly, wave optics refines this picture, but presented considerations provide reliable guidelines, as can be seen in Fig. 4a below.

3 Substrate influence

Often the microspheres are deposited on the substrate being processed [1–3]. Its presence may strongly alter the field distribution, as was studied numerically by the Multiple Multipole method [1] and on the basis of semianalytical Particle-On-Surface method [9, 10]. The influence of the Si substrate on the focusing by the *small* SiO$_2$ microspheres can be seen in Figs. 2c, 3c, which shall be compared with the Figs. 2a, 3a. The parameters correspond to those in Ref. [3]. In Fig. 2 one can see significant shift in the position and increase in the value of maximum intensity inside the sphere. At the

same time, Fig. 3 shows significant decrease in peak intensity flowing into the substrate. Another interesting feature is slight narrowing of the S_z distribution perpendicular to polarization direction, which is opposite to the typical elongation of the field intensity (not shown) [18, 19].

Let us qualitatively illustrate the influence of the substrate. We shall treat all surfaces and wavefronts near the sphere-substrate interstice as plane, and neglect the influence of the back surface of the sphere. Then the gap between the sphere and the substrate can be considered as a Fabry-Perot (FP) resonator with the mirrors R and R_s. Here R and R_s are Fresnel intensity reflection coefficients on the sphere-gap and gap-substrate interfaces, respectively. Let us denote z-component of the Poynting vector, S_z, inside the sphere, just before the last interface as I_0. *Without* the substrate the intensity behind the sphere is then $I_M = (1 - R)I_0$ ("M" stands for "Mie"). The intensity flowing into the substrate, I_S, can be estimated as the transmission of a FP resonator [17]:

$$I_S = \frac{(1 - R_s)(1 - R)}{(1 - \sqrt{RR_s})^2 + 4\sqrt{RR_s}\sin^2\psi/2} I_0$$

$$\leq \frac{1 - R_s}{(1 - \sqrt{RR_s})^2} I_M. \quad (7)$$

Here ψ is the round-trip phase in the resonator. The last inequality gives the upper bound in terms of Mie intensity I_M. It is achieved at $\psi = \pi m$, m being integer. The FP does not necessarily operate at normal incidence. Large angles are needed to account for the large axial component of the electric field E_z behind the sphere mentioned in Sect. 2. This modifies the reflection coefficients and the round-trip phase. But for the wide range of parameters, small vacuum gap ($\psi \to 0$) corresponds to maximum in transmission.

One can see, that I_S may both increase and decrease with respect to I_M. For example, with "symmetric FP" where $R_s = R$, one obtains $I_S/I_M \leq 1/(1 - R)$ and an *increase* in S_z behind the sphere is expected. Conversely, if $R \ll 1$, $R_s \sim 1$, which is the case for the SiO$_2$ sphere on Si substrate, one obtains $I_S/I_M \leq 1 - R_s$, i.e., the *decrease* in the energy flow into the substrate is expected due to strong reflection.

One should differentiate between the energy flow components, such as S_z, and the local energy density, such as EE^*. The latter can increase multifold, as in a FP resonator with high Q-factor. It may also contain phase-sensitive interference pattern (primarily due to light reflected from the substrate), while the energy flow is a more robust quantity, which varies less with the small changes in parameters and geometry.

For the material parameters listed in the caption to Fig. 2, $R = 0.024$ for SiO$_2$ and $R_s = 0.735$ for Si at normal incidence. The actual field includes rays with different angles of incidence and polarizations. For a representative

Fig. 2 Influence of the substrate and lattice neighbors. Energy density defined as $|\operatorname{Re}\varepsilon|\boldsymbol{E}\boldsymbol{E}^*/2$ in the yz-plane. Incident x-polarized plane wave with $E=1$ propagates from right to left. Figure center is at $\boldsymbol{r}=(0,0,a)$. Laser wavelength $\lambda=266$ nm, sphere radius $a=150$ nm, which corresponds to the Mie parameter $ka=3.543$. Refractive index of the spheres $n_{SiO_2}=1.36$. $\varepsilon_{Si}\equiv n_{Si}^2=(1.831+4.426i)^2=-16.24+16.21i$. Nearest neighbors in (**b**) and (**d**) are along the x-axis. (**a**) Single sphere in vacuum, (**b**) seven spheres in vacuum, (**c**) single sphere on Si, (**d**) seven spheres on Si. In (**c**) and (**d**), the position of the Si substrate is indicated by an *arrow*
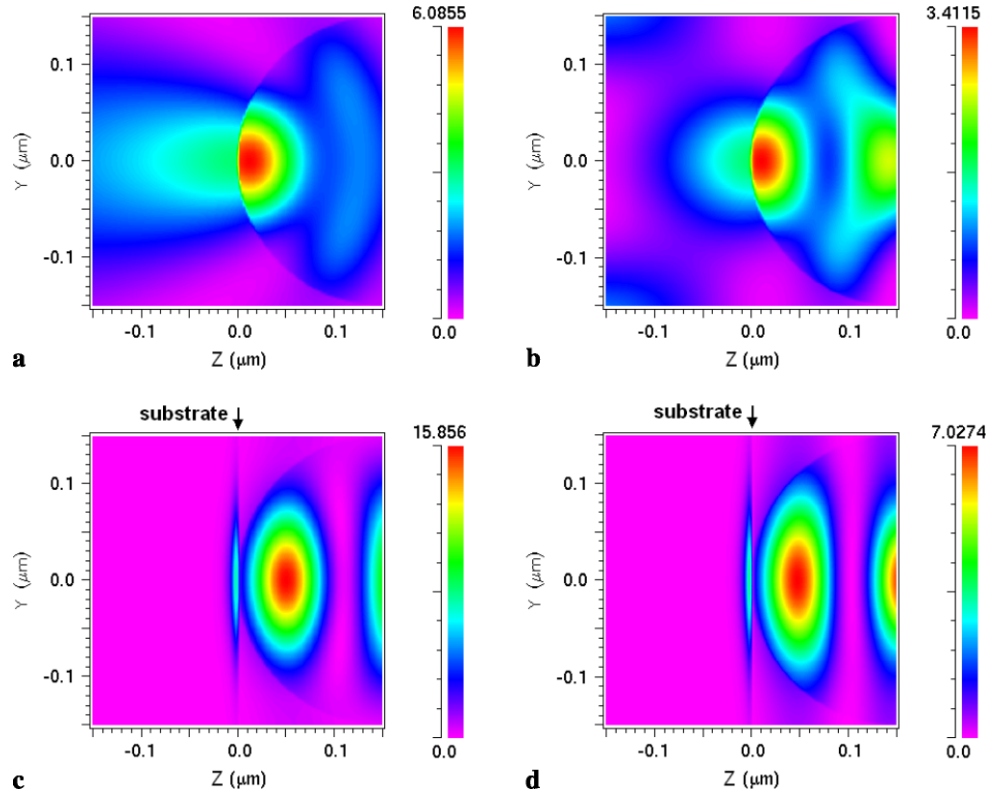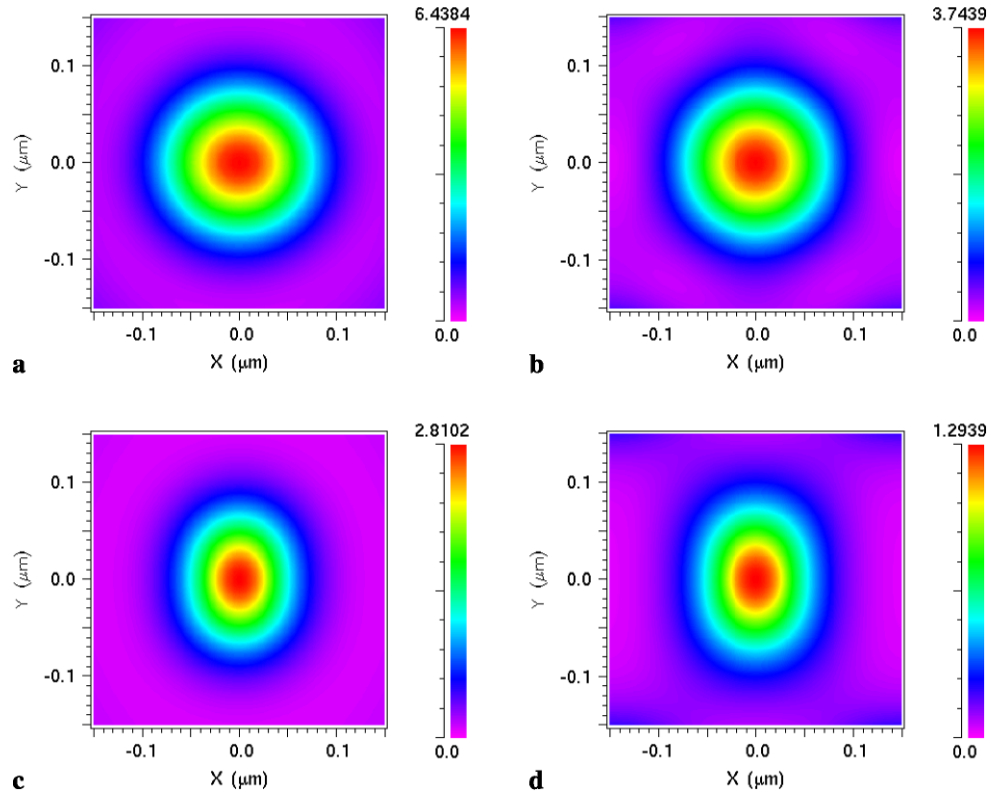

Fig. 3 Distribution of the z-component of Poynting vector, S_z, in the xy-plane immediately behind the sphere. It is normalized to its value in the incident plane wave. Parameters are as in Fig. 2. (**a**) Single sphere in vacuum, (**b**) seven spheres in vacuum, (**c**) single sphere on Si, (**d**) seven spheres on Si

large vacuum angle $\beta=1$, (polarization average) $R=0.054$ and $R_s=0.714$. Equation (7) yields $I_S/I_M\leq 0.35$ and $I_S/I_M\leq 0.44$ for these two cases. From the FDTD results in

Figs. 3a, c one finds $I_S/I_M=0.426$. The agreement remains reasonable (0.328 for FDTD) with small liftoff distance $h=30$ nm, which removes geometrical singularities. To

Fig. 4 Influence of the metal layer. Energy density $|\operatorname{Re}\varepsilon|\boldsymbol{E}\boldsymbol{E}^{*}/2$ in the yz-plane. Incident x-polarized plane wave with $E=1$ propagates from right to left. Figure center is at $\boldsymbol{r}=(0,0,a)$. Laser wavelength $\lambda=800$ nm, sphere radius $a=2$ μm, which corresponds to the Mie parameter $ka=15.708$. Refractive index of the spheres $n_{SiO_2}=1.36$. Thickness of the gold layer $h=120$ nm. $\varepsilon_{Au}\equiv n_{Au}^2=(0.181+5.125i)^2=-26.23+1.855i$. Nearest neighbors in (**b**) and (**d**) are along x-axis. (**a**) Single sphere in vacuum, (**b**) seven spheres in vacuum, (**c**) single metal-covered sphere in vacuum, (**d**) seven metal-covered spheres on quarts support with $n_{quartz}=1.4$. Trigonally-shaped gold islands exist on support between the spheres
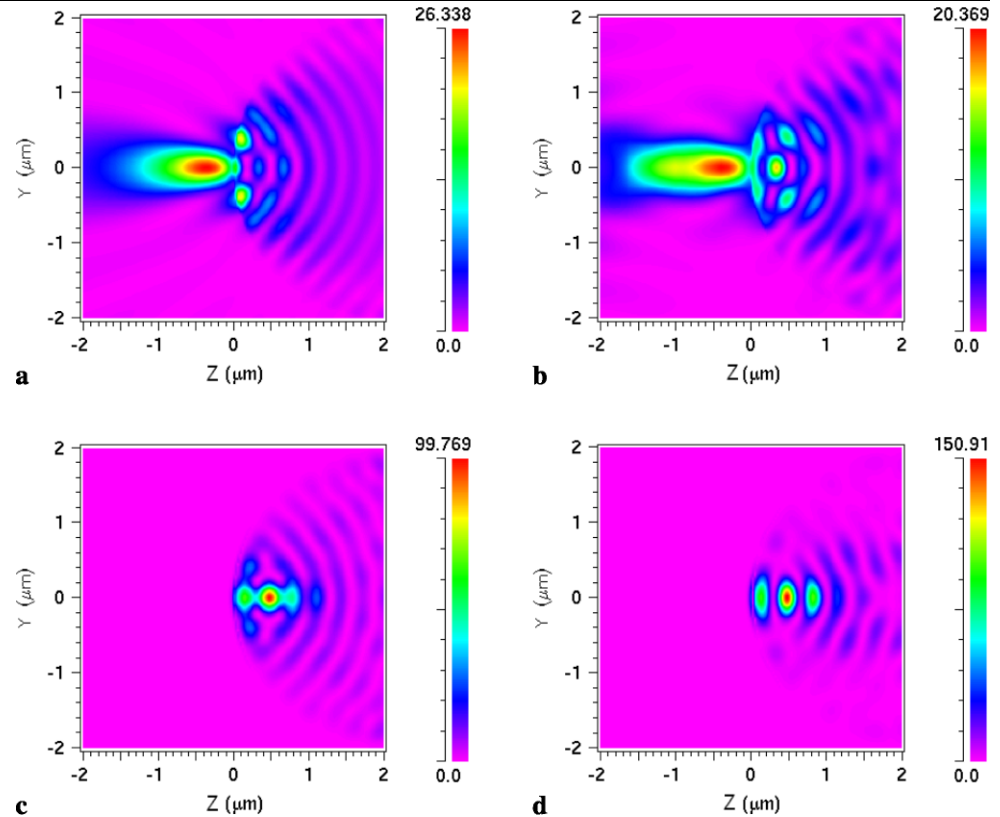
check the FP approximation (7), we also performed the calculations for the symmetric case, $R_s=R$ (quartz substrate). Here the expected ratio is $I_S/I_M \leq 1.024$ and $I_S/I_M \leq 1.058$ for $\beta=0$ and 1, while FDTD yields 1.097 for $h=0$ and 1.01 for $h=30$ nm.

Let us outline two limiting cases for small spheres. The sphere with $ka \ll 1$ lying on a substrate can be considered as a dipole together with its mirror image. In the retarded case one can introduce effective polarizability tensor for arbitrary materials' parameters [21] and ultimately obtain the analytical expressions.

For small isolated particle with large liftoff distance, one can introduce Mie intensities behind and before the particle, $I_{M\pm}$. Such particle only slightly disturbs the incident wave on the substrate. The reflected wave falls onto the particle from the opposite side, and, due to linearity of Maxwell equations, interacts with the particle independently, producing the intensities behind and before the particle with respect to the reflected wave, $I'_{M\pm}=R_s I_{M\pm}$. The *total energy flow* just behind and before the particle in the presence of the substrate are then $I_{S\pm}=I_{M\pm}-I'_{M\mp}=I_{M\pm}-R_s I_{M\mp}$. These approximations were tested numerically, producing reasonable agreement.

Presented results differ from the maximum values of the S_z in the substrate reported in [3]. This may have several reasons. The exact FDTD calculations in the vanishingly thin air gap between the sphere and the substrate require increasingly small spatial (and temporal) resolution. Macroscopic description of the material properties for such a gap is not necessarily justified. Spatial averaging of the dielectric function implemented in the RSoft™ FullWave™ FDTD algorithm can be more physical. FDTD calculations were checked for convergence and compared with Mie and Fresnel solutions. The numerical inaccuracy is about 5% for Figs. 2, 3, 5 and below 20% for Fig. 4. Qualitative features of the field distribution have high degree of reliability. The computational region was $1.25a$ (+PML (perfectly matched layers) of 0.5λ) from the center of the sphere in all directions and $2a$ in the direction of propagation z behind the sphere. In Fig. 5 only the first quadrant of xy-domain was used with symmetric boundary conditions at $x=0$, $y=0$. In all (b), (d) figures with seven spheres hexagonally close-packed in the xy-plane, the domains were extended to $3.25a$ in these directions. Grid size was 64 points per sphere radius with 128 and more in convergence tests.

4 Metallic overlayer

Transmission properties of monolayers with metallic [13, 22] or non-metallic [6, 23] films sputtered on top of microspheres were recently investigated. Metallic films were also used for LIFT (laser induced forward transfer) [7] and formation of small apertures [8, 24]. Focusing properties and

Fig. 5 Influence of capillary condensation. Figure origin $(0, 0, 0)$ is at $\boldsymbol{r} = (0, 0, a)$. Single SiO_2 sphere on Si. (**a**), (**b**) Kelvin radius $R_K = 10$ nm ($RH = 0.95$). (**c**), (**d**) $R_K = 50$ nm ($RH = 0.99$). (**a**), (**c**) Energy density $|\operatorname{Re}\varepsilon|\boldsymbol{EE^*}/2$ in the yz-plane. The positions of the Si substrate and water meniscus are indicated by the arrows. (**b**), (**d**) z-component of Poynting vector, S_z in the xy-plane. Refractive index of the water meniscus $\varepsilon_{H_2O} \equiv n_{H_2O}^2 = (1.386 + 7.4 \times 10^{-9}i)^2 = 1.921 + 2.05 \times 10^{-8}i$. Other laser and material parameters are as in Figs. 2, 3
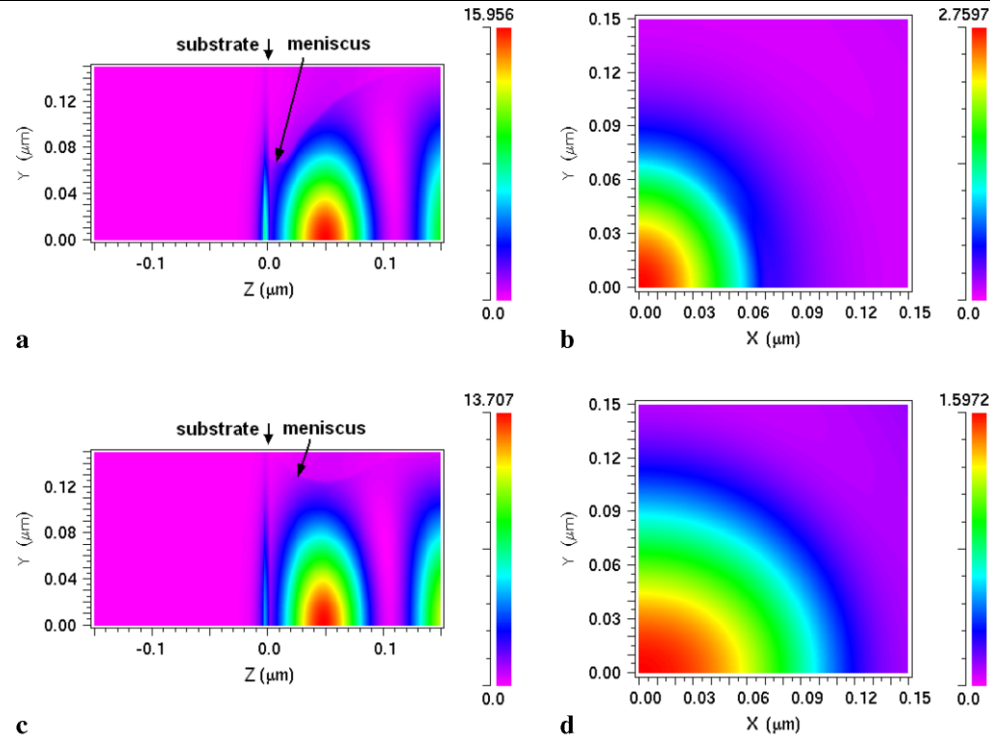
maximum field enhancement have not yet been studied in detail for such geometry. Individual bare and metal-covered spheres are shown in Figs. 4a, c. The parameters are similar to those used in Ref. [8]. One sees more than twofold increase in the maximum field intensity (maximum $\boldsymbol{EE^*}$ values in Figs. 4a, c are 52.7 and 107.9). For the metal-covered sphere it is achieved inside the sphere. This is easily understood along the following lines. Without the metal layer the light is focused outside the sphere. Metal reflects already significantly focused incident light with the reflection coefficient ~ 1. The reflected rays are further focused and interfere with the incoming light, forming a pattern similar to a standing wave. For two equal counter-propagating *plane* waves the maximum field is doubled and $\boldsymbol{EE^*}$ quadrupled. This is indeed the case near the metal surface (but not *on* it!). As incident and reflected waves are unevenly focused, their amplitudes differ inside the sphere and the global maximum enhancement is lower. In a more detailed treatment one can describe the focusing of both incoming and reflected rays with Bessoid matching from [12] and consider their interference.

As with the reflecting substrate in Sect. 3, the qualitative features of the field distribution on the sphere surface, such as caustic ring and the focal line (leading to a hot spot on the surface) persist. But the *magnitude* of the flow of energy into the metal, S_z, decreases compared to Mie-based estimations. The on-axis field contains contributions from the axial ray at normal incidence and the cone of abaxial rays responsible for high intensity $\propto ka$ (Sect. 2). The former exists for

all parameter values, while the latter is present on the sphere surface only if $n > \sqrt{2}$. For $n = 1.36$ in Fig. 4 the focal line starts slightly outside the sphere, but the contribution from abaxial rays still exists, due to finite wavelength (moderate Mie parameter). The angle of incidence on the metal near the central area (see Fig. 1) is close to $\theta_t = 47.3°$ (total internal reflection for the quartz). Polarization averaged reflection coefficients at the quartz–gold surface are $R_m(0) = 0.963$ and $R_m(\theta_t) = 0.964$. Thus, one can expect for the flow of energy into the metal $I_m/I_M \sim 1 - R_m \approx 0.0365 \ll 1$. Calculations (not shown) confirm this prediction with the accuracy of about 20% (which improves with finer mesh size).

One *does not* see any surface plasmon effects on the outer surface of metal (even for the optimal metal thickness). This is because the rays entering the uncovered sphere leave it at the same angle of incidence. To excite a surface plasmon in Kretschmann configuration the ray at the quartz–air interface should have an angle θ_t in Fig. 1 larger than that of total internal reflection. This is impossible, as the corresponding rays do not enter the sphere.

5 Neighboring spheres

In a typical experiment microspheres are deposited onto the substrate or transparent support in a self-assembly process, resulting in hexagonal ML [1, 3–5, 9]. This may impose similar symmetry on the field distribution in the substrate plane or on the sphere surface [24]. Here we concentrate on

the influence of neighboring spheres on *focusing* properties. Seven spheres in close-packed hexagonal arrangement were used in calculations presented in plots (b), (d) in Figs. 2–4. For small spheres considered in Figs. 2, 3 the maximum field intensity EE^* as well as the Poynting flow behind the sphere, S_z, decrease about twice. This occurs both in vacuum and with the Si substrate present.

For larger spheres in Fig. 4 the situation is even trickier. For bare spheres the field intensity EE^* in the focal region also decreases (Figs. 4a, b), while for metal-covered spheres the opposite effect is observed. In the former case S_z in the focal region decreases as well. In both cases the changes in focal intensity are appreciable. A *decrease* of the field in the focal region is somewhat surprising. It is due to the rays reflected at grazing angles (that is, with high reflection coefficients) from the neighboring spheres and entering the "central" sphere almost at normal incidence (i.e., with high transmission). Their interference with the primary rays results in significant redistribution of energy flow, even in the focal region. The ensuing changes are sensitive to the phases of different rays and can be quite complex, especially in the transverse plane [24].

6 Capillary condensation

If the laser cleaning or nano-patterning experiments are performed in the humid ambient air atmosphere, water meniscus is often formed between the particle and the substrate due to capillary condensation [15]. So-called Kelvin radius R_K (inverse sum of principle curvatures) is given by $R_K \approx \frac{0.52 \text{ nm}}{\ln(RH^{-1})}$, where RH is the relative humidity. For typical numbers R_K is close to meridional radius of the meniscus (this is the radius in the plane of Figs. 5a, c). We used this approximation and assumed complete wetting of the Si substrate and SiO_2 particle. The results of such calculations are presented in Fig. 5, which can be directly compared with Figs. 2c, 3c. One can see the water meniscus in Figs. 5a, c. With high values of RH, when R_K becomes large (Figs. 5c, d) the peak flow of energy into the substrate decreases almost twice, accompanied by significant delocalization of the field enhancement zone. For smaller values of R_K (Figs. 5a, b) this effect is less pronounced, but still exists. This can be qualitatively understood as "defocusing" due to almost complete vanishing of the second refraction, because the refractive index n_{H_2O} is close to n_{SiO_2} at this wavelength. The peak intensity inside the sphere has non-monotonous dependence on R_K. One does not observe strong electric field inside the water itself, but it can be easily heated by the heat transfer from the substrate. The efficiency of this process may increase with R_K due to larger area covered by the water and wider effective "spot size" on the substrate.

7 Conclusions

Focusing properties of transparent microspheres with Mie parameters $ka \geq 30$ can be understood on the basis of uniform asymptotics of geometrical optics. Lateral localization of the field behind the sphere is better than that of the ideal lens and can be understood using the concept of caustic phase shifts.

Substrate may strongly modify the intensity under the sphere. Observed changes can be qualitatively understood treating the interstice between the particle and the substrate as a FP resonator. Energy flowing into strongly reflecting substrate is significantly lower than expected from the estimations based on Mie results.

Similarly, metallic layer deposited atop of large spheres acts as a reflecting mirror. This strongly increases the peak field intensity inside the sphere, but drastically decreases the flow of energy into the metal as compared to Mie-based estimations. This may lead to sphere damage and is important for the analysis of LIFT process in such arrangement.

Apart from modifying the field distribution in the planes parallel to the ML, the close-packed hexagonal arrangement of spheres may noticeably change the intensity both in the focal area and inside the microspheres. For parameters used in this work, when neighboring spheres were included in calculations, the peak on-axis intensity decreased for small bare spheres with or without the substrate, but increased for the larger spheres, when they were metal-covered.

Capillary condensation between the particle and the substrate may lead to a significant decrease of the energy flow into the substrate and delocalization of the high-field region.

These findings show that the field enhancement values obtained from the Mie theory or from the more advanced semi-analytical models should be applied cautiously to a quantitative analysis of the real experimental situations.

References

1. H.J. Münzer, M. Mosbacher, M. Bertsch, O. Dubbers, F. Burmeister, A. Pack, R. Wannemacher, B.U. Runge, D. Bäuerle, J. Boneberg, P. Leiderer, Proc. SPIE **4426**, 180 (2002)
2. S.M. Huang, M.H. Hong, B.S. Luk'yanchuk, Y.W. Zheng, W.D. Song, Y.F. Lu, T.C. Chong, J. Appl. Phys. **92**(5), 2495 (2002)
3. D. Brodoceanu, L. Landström, D. Bäuerle, Appl. Phys. A **86**(3), 313 (2007)
4. R. Denk, K. Piglmayer, D. Bäuerle, Appl. Phys. A **74**(6), 825 (2002)
5. D. Bäuerle, K. Piglmayer, R. Denk, N. Arnold, Lambda Highlights **60**, 1 (2002)

6. L. Landström, N. Arnold, D. Brodoceanu, K. Piglmayer, D. Bäuerle, Appl. Phys. A **83**(2), 271 (2006)

7. L. Landström, J. Klimstein, G. Schrems, K. Piglmayer, D. Bäuerle, Appl. Phys. A **78**(4), 537 (2004)

8. G. Langer, D. Brodoceanu, D. Bäuerle, Appl. Phys. Lett. **89**(26), 261104 (2006)

9. B.S. Luk'yanchuk, M. Mosbacher, Y.W. Zheng, H.J. Münzer, S.M. Huang, M. Bertsch, W.D. Song, Z.B. Wang, Y.F. Lu, O. Dubbers, J. Boneberg, P. Leiderer, M.H. Hong, T.C. Chong, in *Laser Cleaning* (World Scientific, Singapore, 2002), p. 103

10. B.S. Luk'yanchuk, Y.W. Zheng, Y.F. Lu, Proc. SPIE **4065**, 576 (2000)

11. N. Arnold, Appl. Surf. Sci. **208–209**, 15 (2003)

12. J. Kofler, N. Arnold, Phys. Rev. B **73**(23), 235401 (2006)

13. L. Landström, D. Brodoceanu, K. Piglmayer, D. Bäuerle, Appl. Phys. A **84**(4), 373 (2006)

14. R. Denk, K. Piglmayer, D. Bäuerle, Appl. Phys. A **76**(1), 1 (2003)

15. N. Arnold, G. Schrems, D. Bäuerle, Appl. Phys. A **79**, 729 (2004)

16. Y.A. Kravtsov, Y.I. Orlov, *Geometrical Optics of Inhomogeneous Media* (Springer, Berlin, 1990)

17. M. Born, E. Wolf, *Principles of Optics: Electromagnetic Theory of Propagation, Interference and Diffraction of Light*, 7th edn. (Cambridge University Press, Cambridge, 1999)

18. H.J. Münzer, M. Mosbacher, M. Bertsch, J. Zimmermann, P. Leiderer, J. Boneberg, J. Microsc. **202**(1), 129 (2001)

19. D. Bäuerle, G. Wysocki, L. Landström, J. Klimstein, K. Piglmayer, J. Heitz, Proc. SPIE **5063**, 8 (2003)

20. J. Kofler, J. Kepler University (2004)

21. D. Bedeaux, J. Vlieger, *Optical Properties of Surfaces* (Imperial College Press, London, 2002)

22. L. Landström, D. Brodoceanu, K. Piglmayer, D. Bäuerle, Appl. Phys. A **81**(1), 15 (2005)

23. L. Landström, D. Brodoceanu, N. Arnold, K. Piglmayer, D. Bäuerle, Appl. Phys. A **81**(5), 911 (2005)

24. A. Pikulin, N. Bityurin, G. Langer, D. Brodoceanu, D. Bäuerle, Appl. Phys. Lett. **91**(19), 191106 (2007)